




Resistive switching mechanisms in BiFeO₃ devices with YBCO and Ag as top electrodes

Santiago Ceballos Medina^{a,b}, Lorena Marín Mercado^{a,b}, Alexander Cardona-Rodríguez^c,
 Mario Fernando Quiñonez Penagos^{a,b}, César Magén^{d,e}, Luis Alfredo Rodríguez^{b,f},
 Juan Gabriel Ramírez^{c,*} 

^a Grupo de Películas Delgadas, Departamento de Física, Universidad Del Valle, A.A. 25360, Cali, Colombia

^b Centro de Excelencia en Nuevos Materiales, Universidad Del Valle, A.A. 25360, Cali, Colombia

^c Department of Physics, Universidad de Los Andes, Bogotá, 111711, Colombia

^d Instituto de Nanociencia y Materiales de Aragón (INMA), Departamento de Física de La Materia Condensada, Universidad de Zaragoza, 50009 Zaragoza, Spain

^e Laboratorio de Microscopía Avanzada (LMA), Universidad de Zaragoza, 50018, Zaragoza, Spain

^f Grupo de Transiciones de Fase y Materiales Funcionales, Departamento de Física, Universidad Del Valle, A.A. 25360, Cali, Colombia

A B S T R A C T

The resistive switching (RS) effect in ferroelectric oxides continues to attract significant attention due to its potential applications in nonvolatile memory and neuromorphic computing devices. In this study, we investigate the RS properties of BiFeO₃/YBa₂Cu₃O_{7-d} (BFO/YBCO) bilayers grown on LSAT substrates, comparing two different top-electrode materials: YBCO and Ag. The devices were fabricated using reactive sputtering at high oxygen pressure, and their RS mechanisms were investigated via current-voltage (I-V) measurements. We find all devices exhibit unipolar behavior, with symmetric RS behavior observed in devices with YBCO top electrodes and asymmetric RS in those with Ag top electrodes. Devices with YBCO top electrodes display ohmic conduction, whereas Ag top electrode devices exhibit a combination of Schottky, Poole-Frenkel emission, and space charge limited conduction mechanisms. Resistance versus time measurements were performed over 30 cycles with 20 different writing voltages to evaluate the ratio between the low resistance state (LRS) and high resistance state (HRS). Ag top electrode devices consistently exhibited higher resistance ratios – approximately three times larger – compared to YBCO devices. Furthermore, better temporal stability of HRS and LRS was observed in devices with Ag top electrodes, attributed to the differences in the Fermi energy levels between YBCO, Ag and BFO. The superior performance of Ag top electrode devices, including their higher storage density and low operation parameters (0.25 V and 5 nA), highlights their potential for energy-efficient applications in future oxide-based memory and neuromorphic devices.

1. Introduction

Resistive random-access memory (ReRAM) devices, which operate based on the resistive switching (RS) effect, have emerged as leading candidates for next-generation memory applications, especially in low-power scenarios [1]. These devices show increasing promise across diverse fields, from biosensors [2–4] and aerospace technologies [5,6] to energy-efficient data centers supporting Internet of Things (IoT) and cloud computing applications [7–9]. Recent advancements have demonstrated that RS-based memristive devices can achieve brain-like computation efficiency, establishing them as pivotal components in energy-efficient neuromorphic computing systems [10–13].

Among various device architectures, the metal-insulator-metal (MIM) capacitor-like structure has emerged as the preferred configuration for implementing RS devices [14], surpassing alternative designs in versatility [15]. This architecture excels not only in conventional

ReRAM applications but also enables crossbar array designs essential for neuromorphic computing implementations [16–18]. The crossbar architecture is particularly advantageous for neural network implementations, as it facilitates efficient parallel processing and synaptic weight storage within a compact form factor.

A fundamental challenge in the field lies in understanding the underlying mechanisms of RS in oxide-based devices. Though researchers have established that RS typically involves filament formation through oxygen vacancy movement [19], the complex interplay among thermal, ionic, and electronic effects during both unipolar and bipolar switching demands further investigation. Particularly crucial is understanding the relationship between vacancy migration and memory retention - the device's ability to maintain its resistance state over time. This retention strongly depends on the ionic interactions at the oxide-electrode interface [20], making the choice of electrode materials a critical design consideration.

* Corresponding author.

E-mail address: jgramirez@uniandes.edu.co (J.G. Ramírez).

<https://doi.org/10.1016/j.physo.2024.100249>

Received 16 September 2024; Received in revised form 26 December 2024; Accepted 28 December 2024

Available online 31 December 2024

2666-0326/© 2024 The Author(s). Published by Elsevier B.V. This is an open access article under the CC BY-NC-ND license (<http://creativecommons.org/licenses/by-nc-nd/4.0/>).

While extensive research has examined elementary metallic electrodes (Al, Pt, Au) with oxides like TiO_x [16,21], the potential of metallic oxides as electrodes remains largely unexplored. This gap is significant because metallic oxide electrodes could provide an additional source of O^{+2} ions for fine-tuning the RS effect. Furthermore, the integration of functional oxides as active layers, particularly multiferroic materials like BiFeO_3 (BFO) [19,22], offers additional opportunities for device optimization [1,27].

BFO has garnered significant attention due to its versatility in multifunctional applications across photonics, electronics, spintronics, and piezotronics [22]. In thin-film form, BFO exhibits complex conduction mechanisms that are not yet fully understood. Previous studies have identified multiple concurrent mechanisms, including filament paths [23,24], Schottky emission [24–26,28], Poole-Frenkel emission [25,26], ohmic conduction [24,26], and space-charge-limited conduction (SCLC) [24,26,28,29]. The presence of these various mechanisms, which can coexist or dominate under different conditions, makes it challenging to optimize device performance. Devices utilizing BFO have achieved resistance ratios of 102–103 [23,26,30–32], with SET and RESET voltages ranging from 3.3 to 5 V [24,26] in various configurations such as Au/BFO/X (X = Nb-doped SrTiO_3 (NSTO), $\text{La}_{1-x}\text{Sr}_x\text{MnO}_3$ (LSMO), SrRuO_3 (SRO) [23], ITO [24] or Pt [25]). Notably, recent work has demonstrated that BFO-based devices can achieve bipolar resistive switching without requiring an initial forming process [33], suggesting promising pathways for simplified device operation and improved reliability.

A fundamental challenge lies in understanding how electrode materials influence these conduction mechanisms, particularly at the interface between BFO and different electrode materials. This understanding is crucial as the electrode choice can determine whether the device operates in bipolar [22,26] or unipolar [26,27] mode, ultimately affecting the dominant conduction mechanism. While numerous studies have investigated RS cycling between high resistance state (HRS) and low resistance state (LRS) in devices like Au/BFO/X [20,21,28], a comprehensive analysis of the relationship between electrode materials, interface properties, and resulting conduction mechanisms remains lacking.

In this work, we address these challenges by investigating DC current-voltage characteristics to determine electronic conduction mechanisms and RS effects in devices utilizing Ag and $\text{YBa}_2\text{Cu}_3\text{O}_{7-d}$ (YBCO) as top electrodes with a BFO thin film active layer. We demonstrate that while YBCO/BFO/YBCO devices with ohmic interfaces exhibit minimal RS effects, the Ag/BFO/YBCO configuration shows enhanced RS effects at the Ag/BFO interface through a combination of ohmic, Poole-Frenkel, and Schottky electronic conduction mechanisms. These results underscore the critical role of electrode material selection in tuning RS performance and highlight the potential of Ag as a top electrode for optimizing BFO-based RS devices.

2. Experimental

We fabricated a set of 4 samples with a capacitor-type structure, employing BFO as the active layer, and YBCO (samples labeled A and A') or Ag (samples labeled B and B') as electrodes. The samples were deposited onto (001)-oriented $(\text{LaAlO}_3)_3(\text{Sr}_2\text{AlTaO}_6)_7$ (or LSAT) substrates. Each pair of samples with the same configuration was fabricated simultaneously. The bottom and top YBCO layers in samples A and A' were fabricated using the DC sputtering technique with a stoichiometric YBCO target, under a 2.5 mbar oxygen atmosphere and a power density of 4.07 W/m^2 . The above parameters yielded YBCO films with a thickness of 85 nm. The BFO layers were grown from a stoichiometric target using RF sputtering technique, under a 0.4 mbar oxygen pressure and a fixed power density of 3.55 W/m^2 , resulting in films of 15 nm thickness. For samples B and B', the BFO/YBCO layers were deposited under the same conditions. Finally, the Ag electrodes were grown in a separate system via thermal evaporation technique, using an evaporation current

of 98 A that allows a deposition rate of 4.5 nm/min until reaching a final thickness of 85 nm.

A nano-scale exploration of the crystal structure and interface of the multilayered systems was carried out by high-resolution transmission electron microscopy (HRTEM) experiments on cross-sectional lamellae fabricated by focused ion beam (FIB) technique. The HRTEM experiments were performed in an image-corrected FEI Titan Cube 60–300 microscope, operated at 300 kV. The RS effect was investigated through a combination of current-controlled and voltage-controlled I - V measurements. The measurement protocol used was based on the procedure reported by A. Cardona et al. [20]. Up to 30 HRS/LRS cycles were performed, employing switching voltages between 0.25 and 5.0 V. The HRS and LRS values were averaged, and their difference (ΔR) was calculated. In addition, the retention time was determined by measuring the time-evolution of the HRS and LRS states.

3. Results and discussion

We first examined the structural characteristics of our devices through detailed microscopy analysis. Fig. 1(a) shows a HRTEM image recorded in a small section of a cross-sectional FIB lamella of the Ag/BFO/YBCO system. Here we see as the sputtering technique facilitated an heteroepitaxial growth of the BFO/YBCO bilayer, resulting in a flat and well-defined interface. However, the Ag electrode exhibited a polycrystalline character, which is typical of microstructures produced by thermal evaporation deposition. An electron diffraction analysis, performed on each system by computing the Fast Fourier Transform (FFT) in selected zones of the HRTEM images, revealed that the YBCO and BFO layers grew with crystal structures corresponding to the $P4/mmm$ [34] and $R3c$ [36] space group, respectively, on the (001)-oriented LSAT substrate. Finally, direct measurements along the films showed that the BFO and YBCO layers have thicknesses close to 15 nm and 85 nm, respectively, closely matching their nominal values.

The energy band diagram of the Ag/BFO/YBCO sample configurations is illustrated in Fig. 2. It is shown that Ag, BFO and YBCO exhibit work function (ϕ) value of 4.6 [37], 4.7 [38] and 6.1 eV [39], respectively (see Fig. 2(a)). BFO also presents an electric affinity of 3.3 eV and a bandgap of 2.8 eV [35]. The interface between BFO and the Ag top electrode and YBCO forms a potential barrier that hinders electron motion due to differences in their Fermi levels. Fig. 2(b) presents the system in forward bias mode, where the Fermi level of BFO is higher than that of Ag and YBCO. This causes upward bending of the valence and conduction bands, characteristic of a Schottky junction. The potential barrier at the BFO/YBCO interface is higher than that of Ag/BFO. Conversely, in reverse bias mode (Fig. 2(c)), the Fermi level decrease, and the junction at Ag/BFO interface becomes ohmic, allowing carriers from Ag to spread into BFO. However, the potential barrier at the BFO/YBCO interface remains high.

Current-controlled and voltage-controlled measurements are shown in Fig. 3, where the current is plotted as density current (J), calculated using the top-electrode area for each sample. The arrows indicate the voltage path followed: $0 \text{ V} \rightarrow 5 \text{ V} \rightarrow 0 \text{ V} \rightarrow -5 \text{ V} \rightarrow 0 \text{ V}$. Two notable observations emerge: (i) all four samples exhibit unipolar RS; (ii) differences in symmetry in the RS behavior arise due to the top electrode material. Thus, samples A and A' (Fig. 3(a) and (b)) show symmetric behavior, while samples B and B' (Fig. 3(c) and (d)) present asymmetric behavior. A rectifier-like behavior, more pronounced in samples B and B', is observed, which can be attributed to the asymmetric energy potential barriers at the Ag/BFO and BFO/YBCO interfaces (See Fig. 2(b) and (c)).

To identify the conduction mechanisms in the samples, we fit the J - V curves employing different established models from the literature [29]. The positive voltage region of the J - V curves in Fig. 3 was used to this analysis, with the fitting results shown in Fig. 4. Ohmic conduction [29] was identified in sample A and A' under positive bias (Fig. 4(a) and (b)), indicating that thermally generated charge carriers within the film

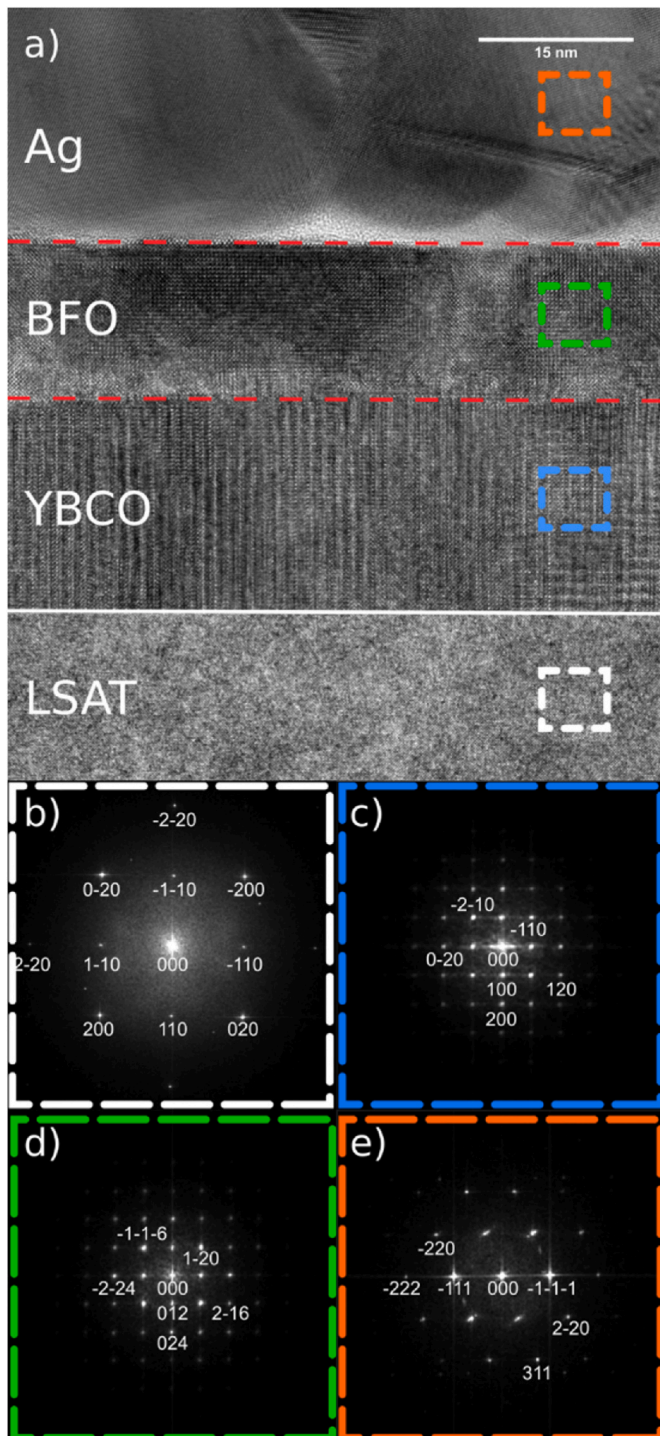


Fig. 1. a) Cross-sectional bright-field TEM image of an Ag/BFO/YBCO device grown on LSAT. FFT diffraction patterns obtained from selected regions of the (b) LSAT, (c) YBCO, (d) BFO and (e) Ag systems (highlighted by the dashed rectangle). The diffraction patterns for YBCO and BFO were indexing assuming crystal structures belonging to the $P4/mmm$ and $R3c$ space groups, respectively.

dominate conduction; the movement of oxygen anions from the ferroelectric oxide towards the positively polarized electrode may occur, resulting in a transition from the HRS to the LRS. When the potential decrease, these oxygen ions are displaced from the interface, generating the observed RS behavior [28].

In sample B and B' (Fig. 4(c) and (d)) we found ohmic conduction, Schottky emission conduction, and Poole-Frenkel emission conduction

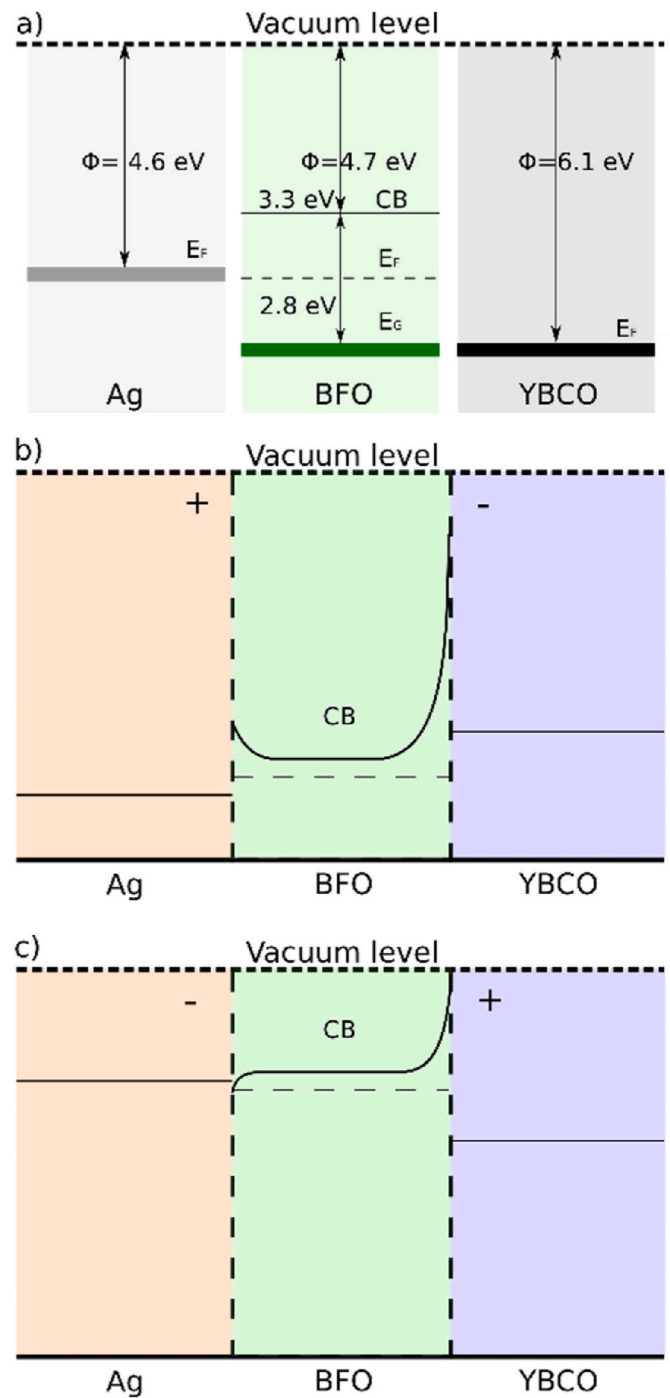


Fig. 2. a) Energy band diagram of Ag, BFO, and YBCO layers, indicating the conduction band (CB) and the Fermi energy level (E_F). Energy band diagram of the Ag/BFO/YBCO system under b) forward and c) reverse bias voltage.

mechanisms. While Schottky emission describes the interface between the top electrode and the dielectric material (Ag/BFO), with its slope corresponding to the barrier height required for charge conduction [29], the presence of Ag as the top electrode introduces additional complexity to the switching mechanism. At the Ag/BFO interface, electrochemical redox reactions of Ag can occur under an applied voltage: Ag atoms can oxidize to Ag^+ ions ($Ag \rightarrow Ag^+ + e^-$) at the anode interface. These Ag^+ ions, being highly mobile, can migrate through the BFO layer under the influence of the electric field, potentially following paths created by oxygen vacancies or other defects. At the cathode interface, these ions can be reduced back to metallic Ag ($Ag^+ + e^- \rightarrow Ag$), contributing to the

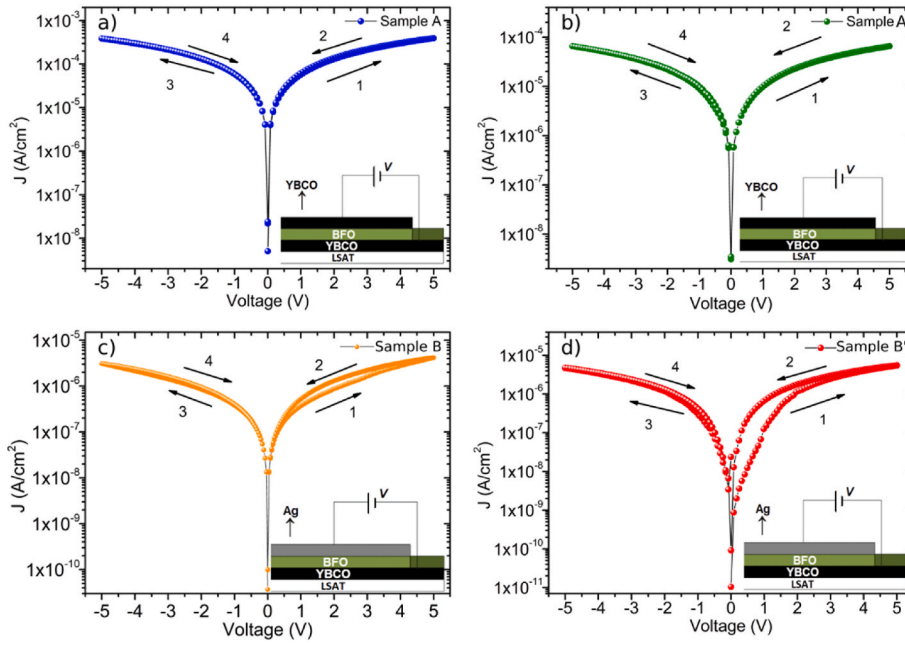


Fig. 3. J-V curves of the samples: a) A, b) A', c) B and d) B'. The insert images represent the system configuration of each sample used during current-controlled and voltage-controlled measurements. Arrows indicate the voltage sweeping sequence path followed by each sample.

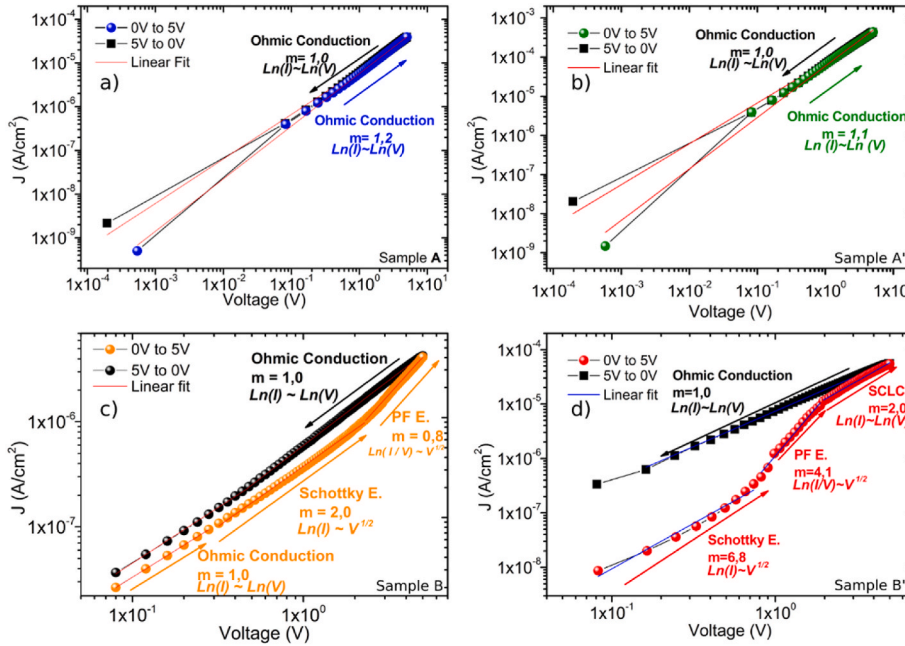


Fig. 4. V curves in a log-log representation for samples with YBCO top electrodes: a) A and b) A', and samples with Ag top electrodes: c) B and d) B', all measured under positive bias.

formation of conductive filaments. This redox-based ion migration mechanism operates alongside the Poole-Frenkel emission observed at higher voltages, which describes conduction of thermally activated charges through traps in the BFO.

The formation of Ag filaments through this oxidation-reduction process can explain several observed phenomena in our devices. First, the enhanced stability of the LRS state in Ag-electrode samples, compared to YBCO samples, can be attributed to the metallic nature of these filaments, which provide stable conductive paths. Second, the remarkable ΔR values (746 % in sample B) may result from the effective modulation of these Ag filaments –their formation leading to LRS and

their partial dissolution or rupture resulting in HRS. The presence of both ionic (Ag^+) and electronic conduction mechanisms creates a complex but more efficient switching process, where the Ag^+ migration complements the oxygen vacancy-mediated switching typically observed in oxide-based devices.

At values close to 5V, where SCLC conduction mechanism predominates, following Child's law [29,40], the high electric field likely enhances both the Ag^+ ion migration and trap-filling processes in BFO [26]. The transition to ohmic conduction in the LRS can be understood as a combination of metallic Ag filament formation and the presence of unfilled traps in the dielectric material, created during the progressive

decrease in the potential difference across the system. This interpretation of multiple concurrent mechanisms—including electronic transport, ionic migration, and electrochemical reactions—aligns with and extends upon previous findings by Chen [27], and Luo et al. [26] in similar asymmetric electrode configurations using BFO.

The cycles with voltage switching between 0.25 and 5.0 V are represented in Fig. 5. We averaged the HRS and LRS values and calculated their difference as $\Delta R = 100 \times (HRS - LRS)/LRS$. Fig. 5(a) shows ΔR as a function of the voltage for sample A. Each data point was calculated from Equation (1) and represents the average of 30 cycles at a specific voltage. As shown in Fig. 5(a) and (b), the highest values of ΔR for the samples A and A' are observed in the voltage range between 2.0 V and 2.75 V. This behavior aligns with previous works [19], where the ordering of ferroelectric domains at 90° occurs once the material is fully polarized at 2.0 V. This voltage range can be described by a local electric field increase in the BFO due to the ordering of its ferroelectric domains, when the device is excited transversely. For the writing process, the optimal voltage was found to be 2.25 V (Fig. 5(a)), with the reset voltage having the same magnitude but inverse polarity. A reading current of $3.21 \mu\text{A}$ was selected as optimal for sample A, while a higher current of $90 \mu\text{A}$ was optimal for sample A'. These results indicate that ΔR values for samples A and A' were 42.1 and 32.5 %, respectively (Fig. 5(b)). In contrast, for samples with Ag top electrode, a writing voltage of 0.25 V and a reading current of 5 (sample B) and 26 nA (sample B') were selected. In these samples, ΔR tended to remain constant as the applied voltage increased. ΔR values for sample B and B' were 746.6 and 140.5 %, respectively. Fig. 6 provides a summary of the optimal parameters identified for each device.

We compared our findings with similar BFO-based devices reported in the literature, as summarized in Table 1. The performance of our Ag/BFO/YBCO device is comparable to or superior to previous studies in terms of the HRS/LRS ratio and operating voltage range. Notably, while most prior studies utilizing noble metal electrodes such as Au and Pt demonstrate bipolar switching behavior, our asymmetric configuration with Ag exhibits stable unipolar switching with a remarkably high ΔR of 746.6 %. This enhancement is attributed to the unique combination of conduction mechanisms, particularly the contribution of Ag^+ ion migration and filament formation, as discussed earlier.

In addition to determining the conduction mechanism, we monitored

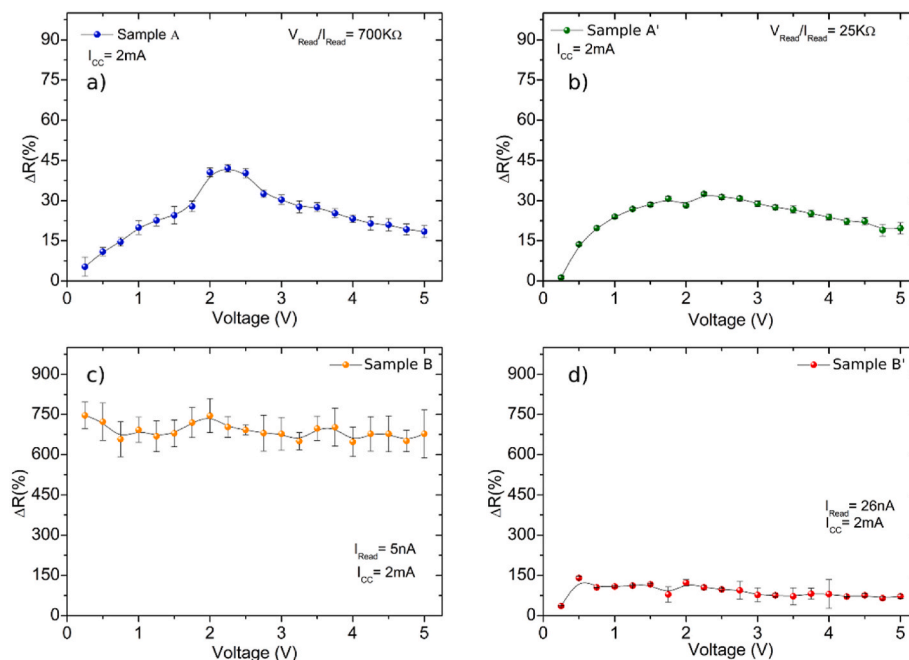


Fig. 5. Resistance ratio (ΔR) for sample with YBCO top electrodes: a) A and b) A', and samples with Ag top electrodes: c) B and d) B'.

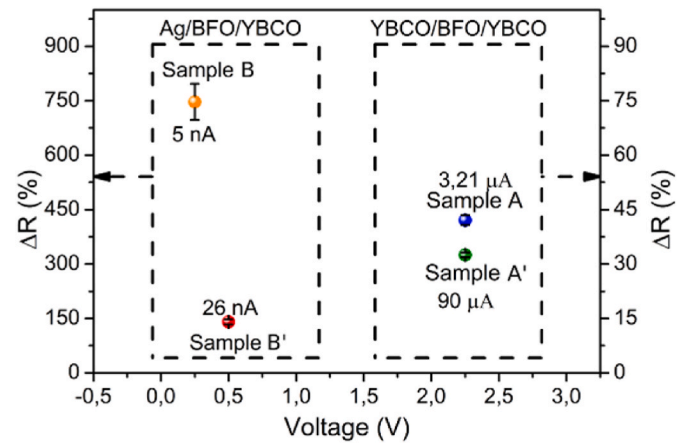


Fig. 6. Summary of the optimal operating parameters identified for the four samples.

the evolution of HRS and LRS over time for samples A and B. Measurements were performed using the previously selected parameters (Fig. 6). Two distinct resistance states are observed in both samples; however, in sample A, these states converge over time. We attribute this behavior to the high mobility of oxygen vacancies between YBCO and BFO layers. In the absence of a potential wall or Schottky barrier to anchor these vacancies, their drift results in a stable state with equal resistance values, causing a loss of the information stored in the device. Understanding the time scales of this process is crucial, as it provides insights into the diffusion rates of vacancies across the layers and their interfaces.

The resistance evolution for sample A, shown in Fig. 7(a), was fitted using a double-exponential decay function:

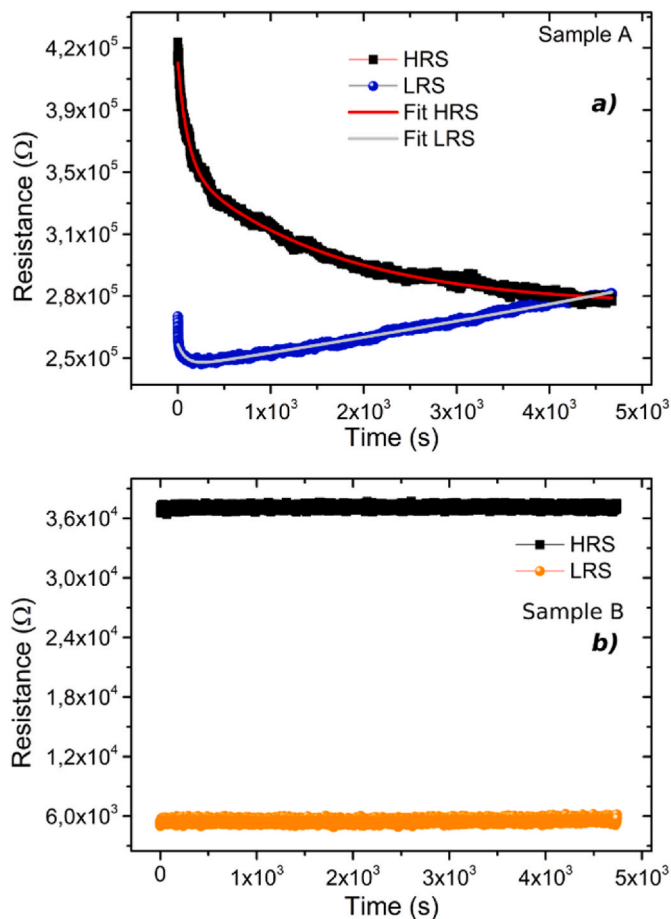
$$R(t) = R_0 + A_1 \exp(-t/\tau_1) + A_2 \exp(-t/\tau_2),$$

where R_0 , A_1 , and A_2 are fitting parameters corresponding to the initial resistance states, and τ_1 and τ_2 are the time constants representing fast and slow relaxation processes for the HRS, respectively. The faster relaxation time, $\tau_1 = 1.7$, is likely due to oxygen vacancy movement or

Table 1

Comparison of resistive switching characteristics in BFO-based devices with different electrode configurations.

Device Structure	RS Type	Conduction Mechanisms	HRS/LRS Ratio (ΔR)	Operating Voltage	Primary Features	Reference
Ag/BFO/YBCO	Unipolar	Ohmic, Schottky, Poole-Frenkel, SCLC	746.6 %	0.25–5.0 V	High stability, Ag filament formation	This work
YBCO/BFO/YBCO	Unipolar	Ohmic	42.1 %	2.25 V	Oxygen vacancy dominated	This work
Au/BFO/NSTO	Unipolar	Filamentary	102–103	3.3–5 V	Domain switching	[21]
Au/BFO/ITO	Bipolar/Unipolar	SCLC, Filamentary	102–103	3–5 V	Mixed conduction	[26]
Au/BFO/Pt	Unipolar	Schottky, SCLC	102	3.3–5 V	Interface-controlled	[27]
Au/BFO/SRO	Bipolar	Schottky emission	102–103	± 4 V	Interface-limited conduction	[22]

**Fig. 7.** Time performance of resistance state for samples: a) A and b) B.

electromigration [41] from the YBCO layer to the BFO. The slower relaxation time, $\tau_2 = 27.0$ min, is attributed to thermal activation processes driven by Joule heating [40].

The analysis of the LRS using the same fitting procedure yielded for $\tau_1 = 1.5$ min and $\tau_2 = 351$ approximately. The comparable τ_1 values between HRS and LRS suggest similar rapid diffusion processes in both states. However, the distinct τ_2 values indicate that Joule heating affects vacancy dynamics differently in the YBCO top and bottom layers, likely due to asymmetric heat dissipation caused by the LSAT substrate acting as a thermal sink. Previous studies have linked such state instabilities to interfacial depolarization effects [40].

In contrast, sample B exhibits superior stability, as shown in Fig. 7 (b), with both resistance states maintaining better separation compared to sample A. This enhanced stability is attributed to the Ag top electrode's distinct properties, including its ionic size and the controlled vacancy mobility at the Ag/BFO interface. The improved retention

characteristics of sample B suggest a robust information storage capability, consistent with previous reports by Wei [42] and Sun [43]. Similar unipolar switching behaviour with asymmetric metal and oxide electrodes has been reported in BFO by Liu [21]. Furthermore, our findings align with Peng's observations [40], where the long-term stability of resistance states was attributed to filamentary conduction. Therefore, we propose that the enhanced stability in our device B likely results from the formation of stable filamentary Ag conduction paths.

4. Conclusions

We have demonstrated resistive switching (RS) behavior in BFO-based devices with two distinct top electrode configurations: YBCO and Ag. Our findings highlight the significant influence of the electrode material on both the conduction mechanisms and the resulting RS characteristics. The Ag top electrode configuration outperforms YBCO due to the favorable potential barrier at the Ag/BFO interface, which facilitates charge transport through optimized Fermi level alignment. All devices exhibit unipolar switching behavior, with interface effects playing a dominant role in the switching mechanism. A particularly notable observation is the rectifier-like behavior, which is more pronounced in devices with Ag top electrodes. The stability of the HRS and LRS states strongly correlates with the choice of top electrode material, with Ag-based devices showing enhanced stability due to the formation of robust conductive filaments within the BFO layer, ensuring reliable retention of information over time. We identified an optimal operating voltage of approximately 2.25 V across all devices, which corresponds to the polarization threshold of the BFO layer. Furthermore, the reproducibility of the driving mechanisms observed in twin samples demonstrates the reliability of our fabrication process. Most notably, the Ag top electrode device (sample B) achieved exceptional performance metrics, including a remarkably high resistance ratio ($\Delta R = 746\%$) and superior temporal stability of both HRS and LRS states. These results, combined with the low operating parameters (reading/writing power), position the Ag/BFO/YBCO device as a promising candidate for next-generation memory applications.

CRedit authorship contribution statement

Santiago Ceballos Medina: Writing – review & editing, Writing – original draft, Investigation, Formal analysis, Data curation. **Lorena Marín Mercado:** Writing – review & editing, Writing – original draft, Supervision, Project administration, Methodology, Investigation, Funding acquisition, Formal analysis, Data curation, Conceptualization. **Alexander Cardona-Rodríguez:** Methodology, Investigation, Formal analysis, Data curation. **Mario Fernando Quiñonez Penagos:** Investigation, Data curation. **César Magén:** Investigation, Formal analysis. **Luis Alfredo Rodríguez:** Writing – review & editing, Writing – original draft, Visualization, Supervision, Methodology, Investigation, Funding acquisition, Formal analysis, Conceptualization. **Juan Gabriel Ramírez:** Writing – review & editing, Validation, Supervision, Project administration, Methodology, Investigation, Funding acquisition,

Formal analysis, Data curation, Conceptualization.

Declaration of competing interest

The authors declare that they have no known competing financial interests or personal relationships that could have appeared to influence the work reported in this paper.

Acknowledgments

Authors acknowledge support from Universidad del Valle under contract No. 71337, and Vicerrectoría de Investigaciones y Facultad de Ciencias from Universidad de los Andes under grant INV-2020-105-2070. The authors appreciate the support from Carlos Arango and Robinson Moreno for assistance on the device fabrication.

Data availability

Data will be made available on request.

References

- [1] X. Zhao, S. Menzel, I. Polian, H. Schmidt, N. Du, Review on resistive switching devices based on multiferroic BiFeO₃, *Nanomaterials* 13 (8) (Apr. 2023) 1325, <https://doi.org/10.3390/nano13081325>.
- [2] X. Zhang, et al., Two-dimensional MoS₂-enabled flexible rectenna for Wi-Fi-band wireless energy harvesting, *Nature* 566 (7744) (2019) 368–372, <https://doi.org/10.1038/s41586-019-0892-1>.
- [3] H.-S.P. Wong, et al., Metal–oxide RRAM, *Proc. IEEE* 100 (6) (Jun. 2012) 1951–1970, <https://doi.org/10.1109/JPROC.2012.2190369>.
- [4] Y. Zha, Z. Wei, J. Li, Recent progress in RRAM technology: from compact models to applications, in: 2017 China Semiconductor Technology International Conference (CSTIC), IEEE, Mar. 2017, pp. 1–4, <https://doi.org/10.1109/CSTIC.2017.7919731>.
- [5] Y. Wang, et al., Highly stable Radiation-hardened resistive-switching memory, *IEEE Electron. Device Lett.* 31 (12) (Dec. 2010) 1470–1472, <https://doi.org/10.1109/LED.2010.2081340>.
- [6] J.S. Bi, et al., The impact of X-ray and proton irradiation on HfO₂/Hf-based bipolar resistive memories, *IEEE Trans. Nucl. Sci.* 60 (6) (Dec. 2013) 4540–4546, <https://doi.org/10.1109/TNS.2013.2289369>.
- [7] S. Tanakamaru, H. Yamazawa, T. Tokutomi, S. Ning, K. Takeuchi, 19.6 Hybrid storage of ReRAM/TLC NAND Flash with RAID-5/6 for cloud data centers, in: 2014 IEEE International Solid-State Circuits Conference Digest of Technical Papers (ISSCC), IEEE, Feb. 2014, pp. 336–337, <https://doi.org/10.1109/ISSCC.2014.6757459>.
- [8] S. Mondal, C.-H. Chueh, T.-M. Pan, High-performance flexible Ni/Sm₂O₃/ITO ReRAM device for low-power nonvolatile memory applications, *IEEE Electron. Device Lett.* 34 (9) (Sep. 2013) 1145–1147, <https://doi.org/10.1109/LED.2013.2272455>.
- [9] B. Whitehead, D. Andrews, A. Shah, G. Maidment, Assessing the environmental impact of data centres part 1: background, energy use and metrics, *Build. Environ.* 82 (December) (Dec. 2014) 151–159, <https://doi.org/10.1016/j.buildenv.2014.08.021>.
- [10] X. Duan, et al., Memristor-based neuromorphic chips, *Adv. Mater.* 36 (14) (Apr. 2024) 2310704, <https://doi.org/10.1002/adma.202310704>.
- [11] S.S. Kundale, et al., Multilevel conductance states of vapor-transport-deposited Sb₂S₃ memristors achieved via electrical and optical modulation, *Adv. Sci.* 11 (32) (Aug. 2024), <https://doi.org/10.1002/advs.202405251>.
- [12] A.C. Khot, et al., Self-assembled vapor-transport-deposited SnS nanoflake-based memory devices with synaptic learning properties, *Appl. Surf. Sci.* 648 (2024) 158994, <https://doi.org/10.1016/j.apsusc.2023.158994>.
- [13] K.A. Rokade, et al., CogniFiber: harnessing biocompatible and biodegradable 1D collagen nanofibers for sustainable nonvolatile memory and synaptic learning applications, *Adv. Mater.* 36 (24) (Jun. 2024) 2312484, <https://doi.org/10.1002/adma.202312484>.
- [14] S. Munjal, N. Khare, Advances in resistive switching based memory devices, *J. Phys. D Appl. Phys.* 52 (43) (Oct. 2019) 433002, <https://doi.org/10.1088/1361-6463/ab2e9e>.
- [15] D. Kumar, R. Aluguri, U. Chand, T.Y. Tseng, Metal oxide resistive switching memory: materials, properties and switching mechanisms, *Ceram. Int.* 43 (May) (Aug. 2017) S547–S556, <https://doi.org/10.1016/j.ceramint.2017.05.289>.
- [16] J. del Valle, J.G. Ramírez, M.J. Rozenberg, I.K. Schuller, Challenges in materials and devices for resistive-switching-based neuromorphic computing, *J. Appl. Phys.* 124 (21) (Dec. 2018) 211101, <https://doi.org/10.1063/1.5047800>.
- [17] S. Ambrogio, et al., Neuromorphic learning and recognition with one-transistor-one-resistor synapses and bistable metal oxide RRAM, *IEEE Trans Electron Devices* 63 (4) (Apr. 2016) 1508–1515, <https://doi.org/10.1109/TED.2016.2526647>.
- [18] D. Ielmini, Brain-inspired computing with resistive switching memory (RRAM): devices, synapses and neural networks, *Microelectron. Eng.* 190 (Apr. 2018) 44–53, <https://doi.org/10.1016/j.mee.2018.01.009>.
- [19] Z. Wang, et al., Resistive switching materials for information processing, *Nat. Rev. Mater.* 5 (3) (Jan. 2020) 173–195, <https://doi.org/10.1038/s41578-019-0159-3>.
- [20] A. Cardona Rodríguez, et al., Resistive switching in multiferroic BiFeO₃ films: ferroelectricity versus vacancy migration, *Solid State Commun.* 288 (October 2018) (Feb. 2019) 38–42, <https://doi.org/10.1016/j.ssc.2018.11.005>.
- [21] Y. Liu, et al., Mechanisms of resistive switching in BiFeO₃ thin films modulated by bottom electrode, *J. Phys. D Appl. Phys.* 51 (2) (Jan. 2018) 025303, <https://doi.org/10.1088/1361-6463/aa9ae4>.
- [22] Y. Shuai, S. Zhou, D. Bürger, M. Helm, H. Schmidt, Nonvolatile bipolar resistive switching in Au/BiFeO₃/Pt, *J. Appl. Phys.* 109 (12) (Jun. 2011) 124117, <https://doi.org/10.1063/1.3601113>.
- [23] A. Wedig, et al., Nanoscale cation motion in TaOx, HfOx and TiOx memristive systems, *Nat. Nanotechnol.* 11 (1) (Jan. 2016) 67–74, <https://doi.org/10.1038/nnano.2015.221>.
- [24] J. Wu, Z. Fan, D. Xiao, J. Zhu, J. Wang, Multiferroic bismuth ferrite-based materials for multifunctional applications: ceramic bulks, thin films and nanostructures, *Prog. Mater. Sci.* 84 (October 2018) (Dec. 2016) 335–402, <https://doi.org/10.1016/j.pmatsci.2016.09.001>.
- [25] B. Sun, et al., ABO₃ multiferroic perovskite materials for memristive memory and neuromorphic computing, *Nanoscale Horiz* 6 (12) (2021) 939–970, <https://doi.org/10.1039/D1NH00292A>.
- [26] J.M. Luo, S.H. Chen, S.L. Bu, J.P. Wen, Resistive switching and Schottky diode-like behaviors in Pt/BiFeO₃/ITO devices, *J. Alloys Compd.* 601 (Jul. 2014) 100–103, <https://doi.org/10.1016/j.jallcom.2014.02.180>.
- [27] S.-W. Chen, J.-M. Wu, Unipolar resistive switching behavior of BiFeO₃ thin films prepared by chemical solution deposition, *Thin Solid Films* 519 (1) (Oct. 2010) 499–504, <https://doi.org/10.1016/j.tsf.2010.08.004>.
- [28] Q. Yang, et al., The transport properties in BiFeO₃/YBCO heterostructures, *J. Alloys Compd.* 646 (Oct. 2015) 1133–1138, <https://doi.org/10.1016/j.jallcom.2015.05.141>.
- [29] F.-C. Chiu, A review on conduction mechanisms in dielectric films, *Adv. Mater. Sci. Eng.* 2014 (2014) 1–18, <https://doi.org/10.1155/2014/578168>.
- [30] Y. Shuai, et al., Control of rectifying and resistive switching behavior in BiFeO₃ thin films, *APEX* 4 (9) (Aug. 2011) 095802, <https://doi.org/10.1143/APEX.4.095802>.
- [31] L. Zhao, et al., Current rectifying and resistive switching in high density BiFeO₃ nanocapacitor arrays on Nb-SrTiO₃ substrates, *Sci. Rep.* 5 (1) (Apr. 2015) 9680, <https://doi.org/10.1038/srep09680>.
- [32] Y. Shuai, et al., Key concepts behind forming-free resistive switching incorporated with rectifying transport properties, *Sci. Rep.* 3 (1) (Jul. 2013) 2208, <https://doi.org/10.1038/srep02208>.
- [33] H.N. Mohanty, A.K. Jena, U. Yadav, A.K. Sahoo, S. Prasad P, J. Mohanty, Tunable multiferroic and forming-free bipolar resistive switching properties in multifunctional BiFeO₃ film by doping engineering, *J. Alloys Compd.* 887 (2021) 161336, <https://doi.org/10.1016/j.jallcom.2021.161336>.
- [34] C.C. Torardi, et al., Structure-property relationships for R_{Ba}2 Cu 3 O x phases, *ACS Sympos* (1987) 152–163, <https://doi.org/10.1021/bk-1987-0351.ch015>, ch. 15.
- [35] J.M. Moreau, C. Michel, R. Gerson, W.J. James, Ferroelectric BiFeO₃ X-ray and neutron diffraction study, *J. Phys. Chem. Solid.* 32 (6) (Jan. 1971) 1315–1320, [https://doi.org/10.1016/S0022-3697\(71\)80189-0](https://doi.org/10.1016/S0022-3697(71)80189-0).
- [36] M.Y. Bashouti, et al., Systematic surface phase transition of Ag thin films by iodine functionalization at room temperature: evolution of optoelectronic and texture properties, *Sci. Rep.* 6 (1) (Feb. 2016) 21439, <https://doi.org/10.1038/srep21439>.
- [37] S. He, et al., Impact of interfacial effects on ferroelectric resistance switching of Au/BiFeO₃/Nb:SrTiO₃ (100) Schottky junctions, *RSC Adv.* 7 (37) (2017) 22715–22721, <https://doi.org/10.1039/C7RA02339A>.
- [38] A. Walkenhorst, et al., Dielectric properties of SrTiO₃ thin films used in high T_c superconducting field-effect devices, *Appl. Phys. Lett.* 60 (14) (Apr. 1992) 1744–1746, <https://doi.org/10.1063/1.107204>.
- [39] S.J. Clark, J. Robertson, Band gap and Schottky barrier heights of multiferroic BiFeO₃, *Appl. Phys. Lett.* 90 (13) (2007) 1–4, <https://doi.org/10.1063/1.2716868>.
- [40] H.Y. Peng, et al., Electrode dependence of resistive switching in Mn-doped ZnO: filamentary versus interfacial mechanisms, *Appl. Phys. Lett.* 96 (19) (May 2010) 192113, <https://doi.org/10.1063/1.3428365>.
- [41] P. Krzyżeczko, X. Kou, K. Rott, A. Thomas, G. Reiss, Current induced resistance change of magnetic tunnel junctions with ultra-thin MgO tunnel barriers, *J. Magn. Magn. Mater.* 321 (3) (Feb. 2009) 144–147, <https://doi.org/10.1016/j.jmmm.2008.08.088>.
- [42] L.L. Wei, et al., Pulse-induced alternation from bipolar resistive switching to unipolar resistive switching in the Ag/AgO x/Mg 0.2 Zn 0.8 O/Pt device, *J. Phys. D Appl. Phys.* 45 (42) (Oct. 2012) 425303, <https://doi.org/10.1088/0022-3727/45/42/425303>.
- [43] H. Sun, Q. Liu, S. Long, H. Lv, W. Banerjee, M. Liu, Multilevel unipolar resistive switching with negative differential resistance effect in Ag/SiO₂/Pt device, *J. Appl. Phys.* 116 (15) (Oct. 2014) 154509, <https://doi.org/10.1063/1.4898807>.